Effect of stacking direction and raster angle on the fracture properties of Onyx 3D printed components: A mesoscale analysis

Simone Sangaletti, María Teresa Aranda *, Luis Távara, Israel García García

Departamento de Mecánica de Medios Continuos y Teoría de Estructuras, Escuela Técnica Superior de Ingeniería, Universidad de Sevilla, Camino de los Descubrimientos s/n, 41092 Sevilla, Spain

ARTICLE INFO

ABSTRACT

3D printing is a technology that has gained increasing importance both in academia and industry for the possibilities offered. Among the many, one of the most appealing is the possibility to choose different printing configurations, tailoring stacking direction, and raster angle. The choice of such parameters deeply influences the structural response, as already shown in the literature. This study aims at providing a deep understanding of the phenomena taking place at the mesoscale level which justify such differences in the fracture behavior. An experimental campaign is carried out with a Single Edge Notch Bending (SENB) specimen printed in Onyx using four different combinations of raster angles and stacking directions. The results are compared in terms of mechanical response, fracture toughness and surface roughness to identify the main driving mechanisms during the fracture process. The same bending test is replicated numerically, aiming at comparing the fracture toughness values obtained experimentally with the ones used in the simulation to match the experimental curves. The study shows that the stacking direction and the raster angle deeply influence the fracture behavior and the mechanical properties of the specimen, along with the fracture toughness and surface roughness. In particular, it is highlighted how improved mechanical behavior can be achieved by printing the specimen in the vertical direction and with a raster angle of 45°/−45°. Moreover, useful fracture toughness values are identified for different combinations of printing parameters by means of a Cohesive Zone Model formulation, providing useful input values for numerical simulations.

1. Introduction

3D printing is a technique that allows the manufacturing of components that can be used during the testing phase or for real-life applications. The advantages of this production process are numerous and lie mainly in the flexibility of the manufacturing process, enabling shapes that are tailored to the needs of the client, and the reduced production time [1,2]. Both in the prototyping phase and in every-day life use of the components, the mechanical behavior of the 3D printed parts is of primary importance, since some of them are used as structural parts. Therefore, it is of utmost significance to thoroughly study the mechanical performance of such components, considering a detailed analysis of the main mechanisms that govern the response of the undamaged component and its failure. This analysis is mandatory to extend the application of this technology to safety-sensitive fields of application, such as aviation [3–6].

Nowadays, 3D printing processes are gaining more and more attention due to the possibility of extending their application to continuous fiber deposition [7,8]. In recent years, several companies, such as

Markforged, or university spin-offs, such as 9T Lab, have been set up focusing on this topic. The advantages of using a continuous 3D printing fiber deposition strategy are multiple, but mostly one deserves the attention of researchers: the ability to create ad hoc fiber deposition paths, tailoring the in-plane fiber direction, a possibility not allowed by classical lamination techniques, which are widely adopted in the industry right now. As a matter of fact, when considering the traditional hand lay-up technique, whose effectiveness deeply depends on the ability of the operator, or the more recent Automated Fiber Placement (AFP), none of these is able to replicate a reinforcement pattern that can be freely chosen by the designer.

In recent years, significant effort has been devoted to the analysis of such reinforced components. The largest contribution in the literature comes from the experimental side. Justo et al. [9] analyzed the properties of the components reinforced with carbon and glass fibers using tensile, bending, and shear tests, showing that the specimens reinforced with continuous fibers exhibited superior mechanical properties relative to those of nonreinforced ones. Pertuz et al. [10]
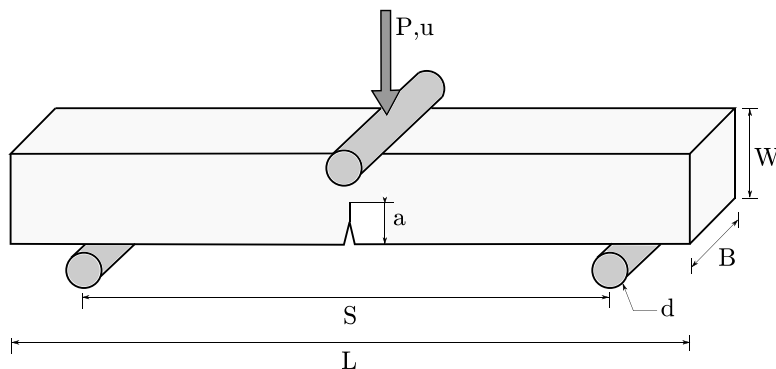

Fig. 1. Schematic of the designed geometry for the single end-notched bending (SENB) specimen.
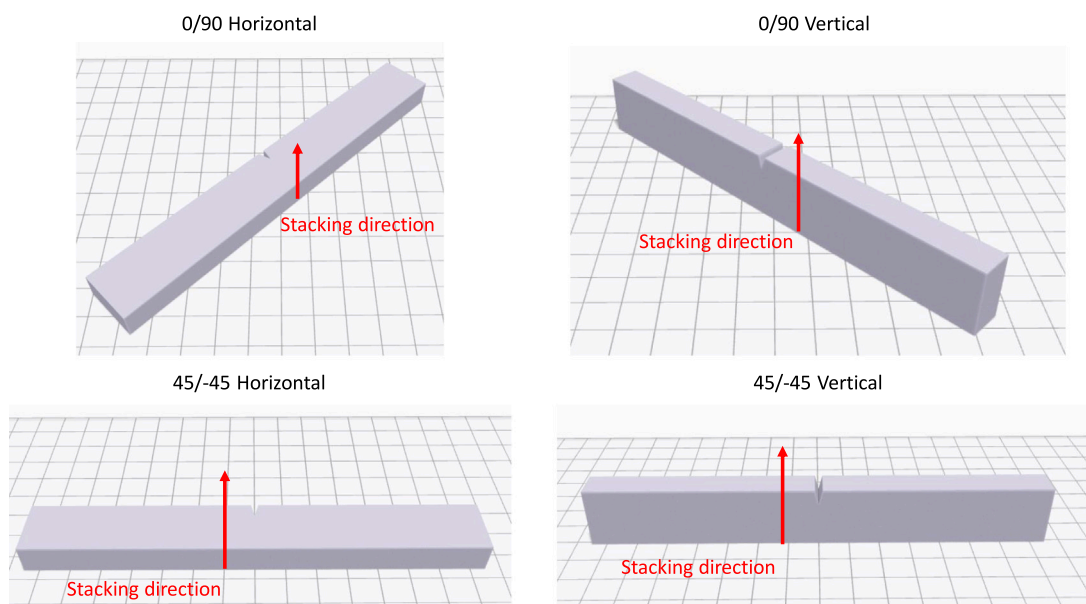

Fig. 2. Specimen configurations associated with the stacking direction and raster angle.

studied the influence of different types of reinforcement fibers (carbon fiber, glass, and Kevlar®) on the static and fatigue behavior of 3D printed specimens. Caminero et al. investigated the influence of process parameters on both interlaminar bonding and impact strength, respectively in [11,12]. Aranda et al. [13] adopted continuous fiber deposition to study the influence on the fracture toughness of structured interfaces in adhesive joints, highlighting a relevant improvement in adhesive performance. Along with experimental work, some authors performed numerical simulations to catch the complex behavior of such 3D-printed structures. Pan et al. [14] applied phase field to study fracture in variable stiffness composites, considering the carbon fiber/epoxy material system and extending the analysis to different geometries, ranging from single edge notch tension to open hole tension simulations. Sangaletti et al. applied the same numerical technique to simulate V-notch and open hole tensile tests using both isotropic [15] and anisotropic [16] formulations.

The scientific contributions described so far deal with continuous fiber reinforcement. This means that a fiber bundle (carbon, glass, or Kevlar®) is deposited by the 3D printed nozzle. The deposition pattern of the continuous fiber is subject to boundaries imposed by the geometry of the specimen to be reinforced. For parts that cannot be filled with reinforcement, Onyx®, a short carbon fiber-reinforced polymeric material, is used. Hence, it is of interest to study the fracture properties of such material as well.

Several authors studied the fracture in additively manufactured components made of polymeric materials from a numerical standpoint.

Li et al. [17] adopted an anisotropic elasto-plastic phase field fracture model to simulate the behavior of coupons printed in Polyamide and with different stress raisers, showing good correlation with experiments. Khosravani et al. [18] applied an anisotropic phase field formulation to study the influence of the raster angle on the strength of tensile coupons printed in PLA, showing good correlation with the experimental campaign performed. Mattey et al. [19] applied an elasto-plastic phase field model to study the influence of the stacking direction on strength and fracture toughness of the printed components. Russ et al. [20] applied again phase field, aiming at the study of the large deformation behavior of composites with soft matrix and stiff inclusions. Estefani and Távara [21] developed a numerical model able to take into consideration the main printing variables for components produced with fused deposition modeling, such as raster angle and porosity.

In addition to the numerical work, various experimental studies have been performed so far. Marsavina et al. [22] studied the fracture toughness for specimens produced in polyamide PA 2200 by laser sintering using different process parameters. In [23], the same authors extended the analysis to different geometries. Cuesta et al. [24] studied the fracture properties of different polymeric materials, including PLA, PP, ABS and Onyx, showing the superior properties of the last one in terms of mechanical resistance. Quan et al. [25] studied the effect of raster angle in 3D printed components made of ABS and fabricated by means of Fused Filament Fabrication (FFF). Chacón et al. [26] studied
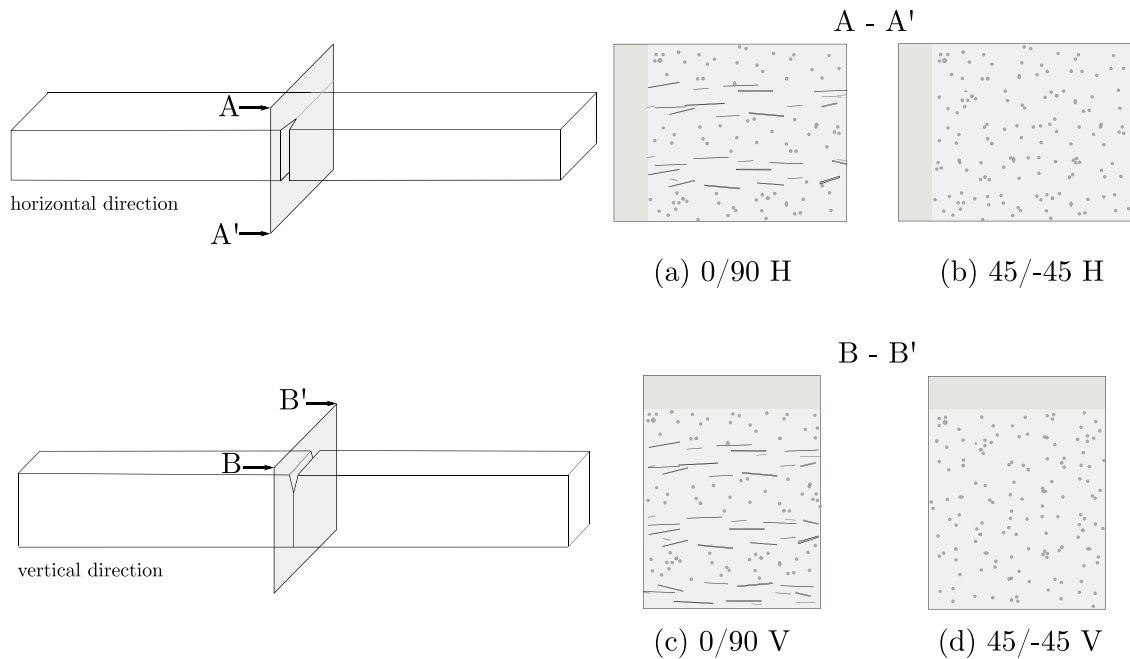
Fig. 3. Expected failure plane and scheme of the lay-up sequence for horizontal and vertical directions.

Fig. 4. Tested SENB specimens for the different configurations: (a) 0/90 Horizontal (b) 0/90 Vertical (c) 45/−45 Horizontal (d) 45/−45 Vertical.

the same effect but for tensile and SENB specimens printed in PLA. Ya-dav et al. [27] examined the same effect in PLA using SENB specimens, considering the effect of the infill pattern and the specimen orientation with respect to the stacking direction, finding a significant influence of these parameters on the fracture toughness. Arbeiter et al. [28] fabri-cated Compact Tension (CT) specimens in PLA to measure the fracture toughness for different raster angles. Aliheidari et al. [29] measured, both experimentally and numerically, the fracture resistance for Double Cantilever Beam (DCB) specimens made of ABS. Zou et al. [30] studied elasticity and yielding performance for tensile specimens printed in ABS, taking into consideration also the effect of the stacking direction. In a more general sense, Khosravani et al. [31] provided a useful review on the post-processing treatments for additively manufactured parts, both in polymer and metal, summarizing their effects on the mechanical properties of such parts. Távara et al. [32] explored the effect on the fracture properties of the raster angle used to deposit Onyx, also paying attention to the aging effect.

Nevertheless, a detailed analysis of the Onyx fracture process at the mesoscale level is missing, trying to explain which are the main causes that lead to a dependence of the mechanical behavior on the raster angle and stacking direction. A deep understanding of these phenom-ena can lead to a better usage of the 3D printing technology itself. Therefore, this work aims to analyze the fracture process at that level of detail, focusing on the fracture surfaces' morphology and roughness

for the different printed specimens. Single Edge Notch Bending (SENB) specimens were fabricated in Onyx using the Markforged MarkTwo 3D printer. Two different raster angles and two different stacking direc-tions were used, leading to a total of four possible combinations, which are eventually compared in terms of mechanical properties and fracture pattern at the mesoscale, justifying what was observed experimentally.

The manuscript is organized as follows: In Section 2, the criteria for the design of the specimen and the fabrication details are explained. In Section 3, the results of the SENB tests are presented, focusing on the morphology of the crack surface and the force–displacement curves obtained. In Section 4, the values of fracture toughness from the experi-mental curves and the roughness of the fracture surfaces are measured. In the same section, the experimental results are replicated numerically using a numerical model that adopts cohesive elements. Eventually, in Section 5, conclusions are drawn, along with the limitations and possible future developments.

2. Specimen design, fabrication and testing

This section describes the design considerations regarding the def-inition and manufacturing of specimens to study the influence on the mechanical response and fracture properties associated to two funda-mental 3D printing parameters: raster angle and stacking direction.
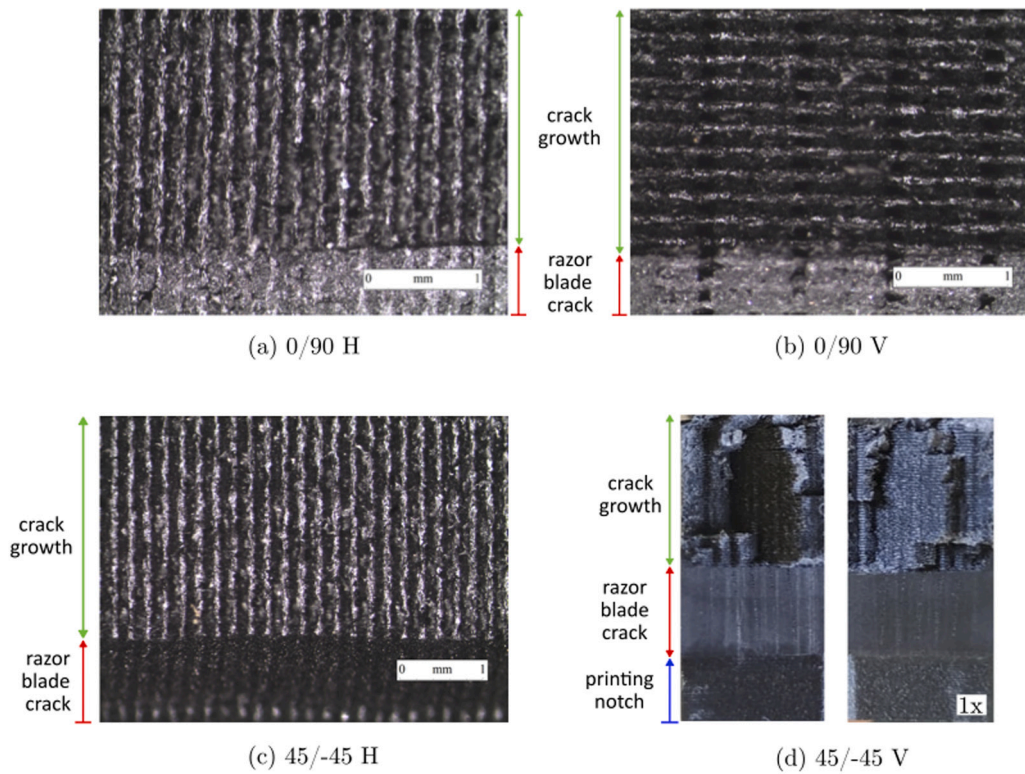
Fig. 5. Fracture surface observations through a microscope for the different configurations: (a) 0/90 Horizontal (b) 0/90 Vertical (c) 45/−45 Horizontal - inclined 45° to follow the crack path (d) 45/−45 Vertical.

A schematic definition of the SENB specimen employed in this study is represented in Fig. 1, according to the specification [33]. The specimen consists of a rectangular beam with a single-edge notch. The specimen is $L = 150$ mm length, with a distance between the bottom roller axes of $S = 80$ mm. The thickness is $B = 10$ mm and crack length is denoted as a. The diameter of the rollers is $d = 15$ mm. An initial notch of 5 mm length is introduced as part of the printed geometry, see Fig. 1. This notch is used to generate a crack using a razor blade. The crack length to be generated with the blade is 5 mm according to the specifications [33], which recommends the total crack length (3D printed notch + natural crack from the razor blade) to be nominally equal to the thickness, B. Therefore, the total crack length is $a = 10$ mm.

The specimens under study are manufactured by fused deposition modeling (FDM), using a Markforged® Mark Two 3D printer and Eiger® CAD software for the definition of the solid model. The material chosen for the specimen fabrication is nylon reinforced with carbon microfibers (Onyx®). The mechanical properties of Onyx® employed are: elastic modulus $E = 2.4$ GPa and Poisson's ratio $\nu = 0.34$, as described by the manufacturer Markforged® and indicated in various papers, such as Estefani and Távara [21]. The nozzle temperature used for the extrusion is 265 °C, which is a fixed parameter in the printer.

The specimens are manufactured following two different stacking directions, as shown in Fig. 2:

(i) Printing in the horizontal direction: the layers are stacked along the thickness direction of the specimen (B). This type of SENB specimen consists of 100 layers with 0.1 mm thickness.

(ii) Printing in the vertical direction: the layers are stacked along the width of the specimen (W). This type of SENB specimen consists of 200 layers each with a thickness of 0.1 mm.

To avoid including any additional effects, every specimen was manufactured using 100% infill. The Markforged Two® printer limits the infill pattern option to 45°/−45° when 100% Onyx infill is required.

This limitation is in line with [34], which suggests using cross-ply patterns to alleviate the effects of pores that appear when a parallel pattern is used. However, it is relevant to analyze the effect of the infill pattern on the global anisotropic behavior of a printed part. In the present study, two different raster angles are used: 45°/−45° and 0°/90°. To obtain printed parts with a 0/90 infill pattern, the part is rotated 45° with respect to the printing bed, as can be observed in Fig. 2.

In total, four different types of specimens are analyzed, combining stacking direction and raster angles: 45/−45 Horizontal, 45/−45 Vertical, 0/90 Horizontal and 0/90 Vertical. These are shown in Figs. 2 and 3.

Five specimens per type were manufactured according to [33], for a total of 20 specimens. Being the specimen made of Onyx, no failure during the printing process has been reported. The displacement is measured along the vertical direction shown in Fig. 1 and the reaction force is measured using a ±5 kN load cell. The velocity of the punching head (10 mm/min) is set in accordance with [33]. The room temperature was optimal for such test and being around 20 °C.

3. Results

This section illustrates the results obtained from the SENB test for all configurations. In the first part, the images of the fracture surface obtained with an optical microscope are shown, along with the digital images obtained with an electronic profilometer. In the following part, the force–displacement curves obtained from the experimental campaign are shown. Based on the results of this section, the critical stress intensity factor K^*, the fracture toughness and the surface roughness are computed and compared in the next one.

3.1. Crack path and fracture surfaces

The images shown in this subsection have been obtained by means of a Nikon optical microscope and a Sensofar digital profilometer,
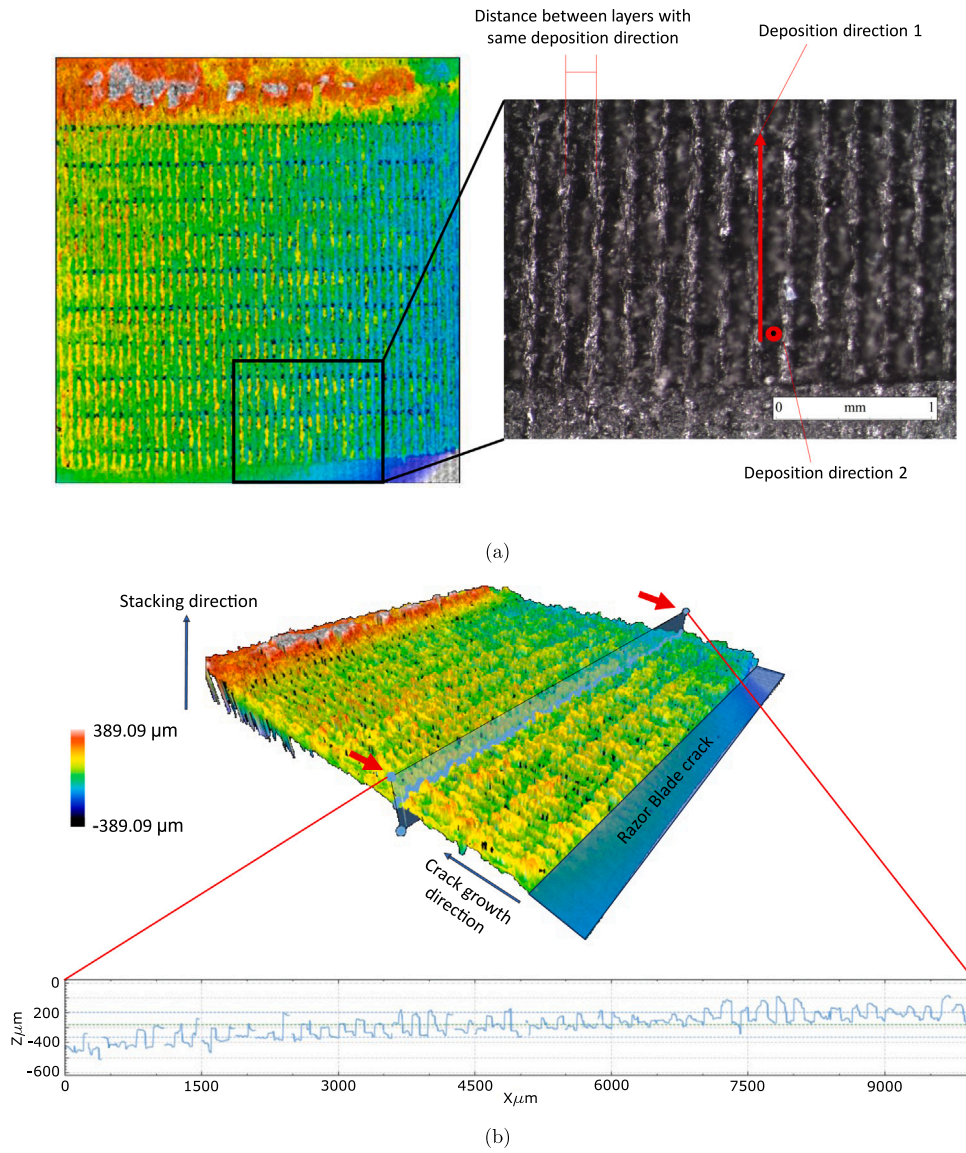
(a)

(b)

Fig. 6. Fracture surface from profilometer and microscope for the 0/90 Horizontal configuration.
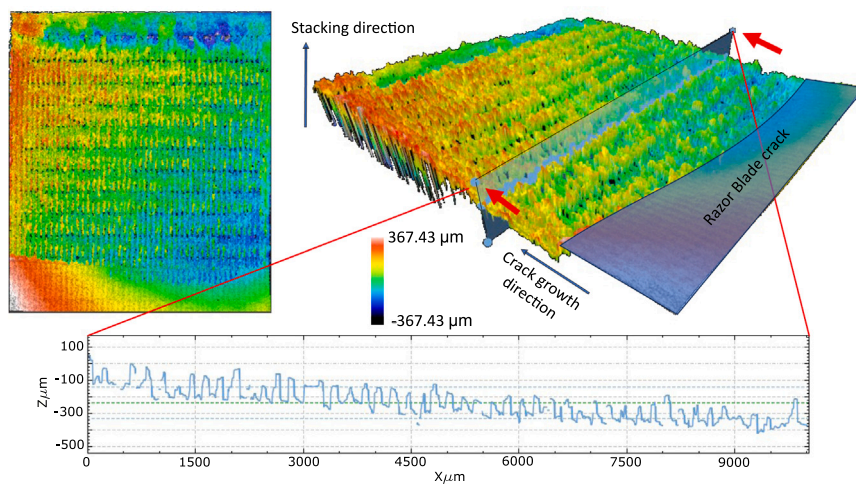

Fig. 7. Fracture surface from profilometer for the 0/90 Horizontal configuration — opposite face.
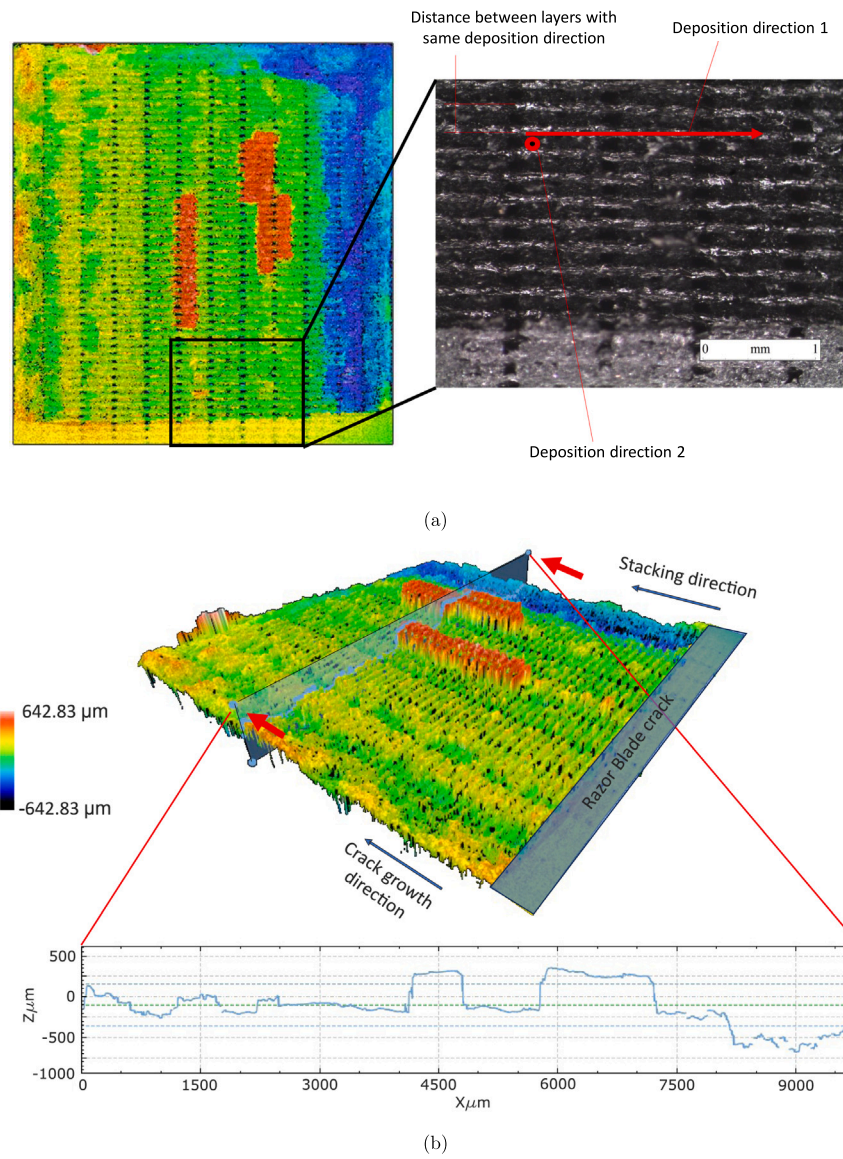
(a)

(b)

Fig. 8. Fracture surface from profiler and microscope for the 0/90 Vertical configuration.
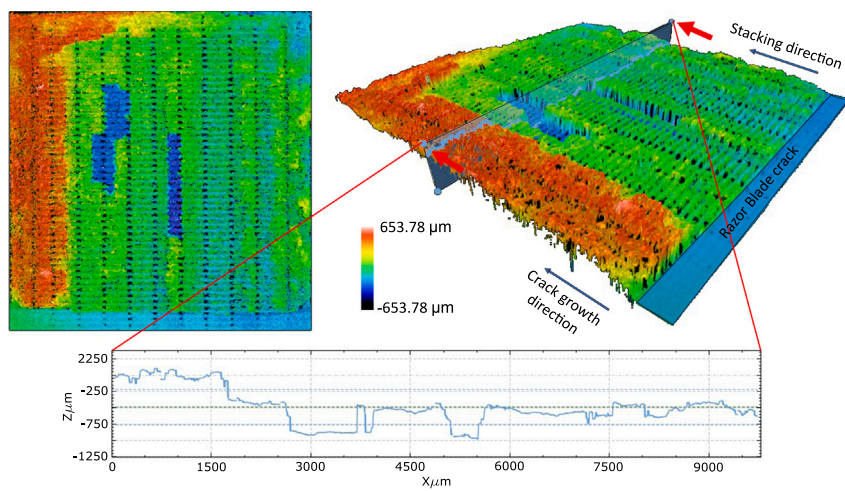

Fig. 9. Fracture surface from profilometer for the 0/90 Vertical configuration — opposite face.
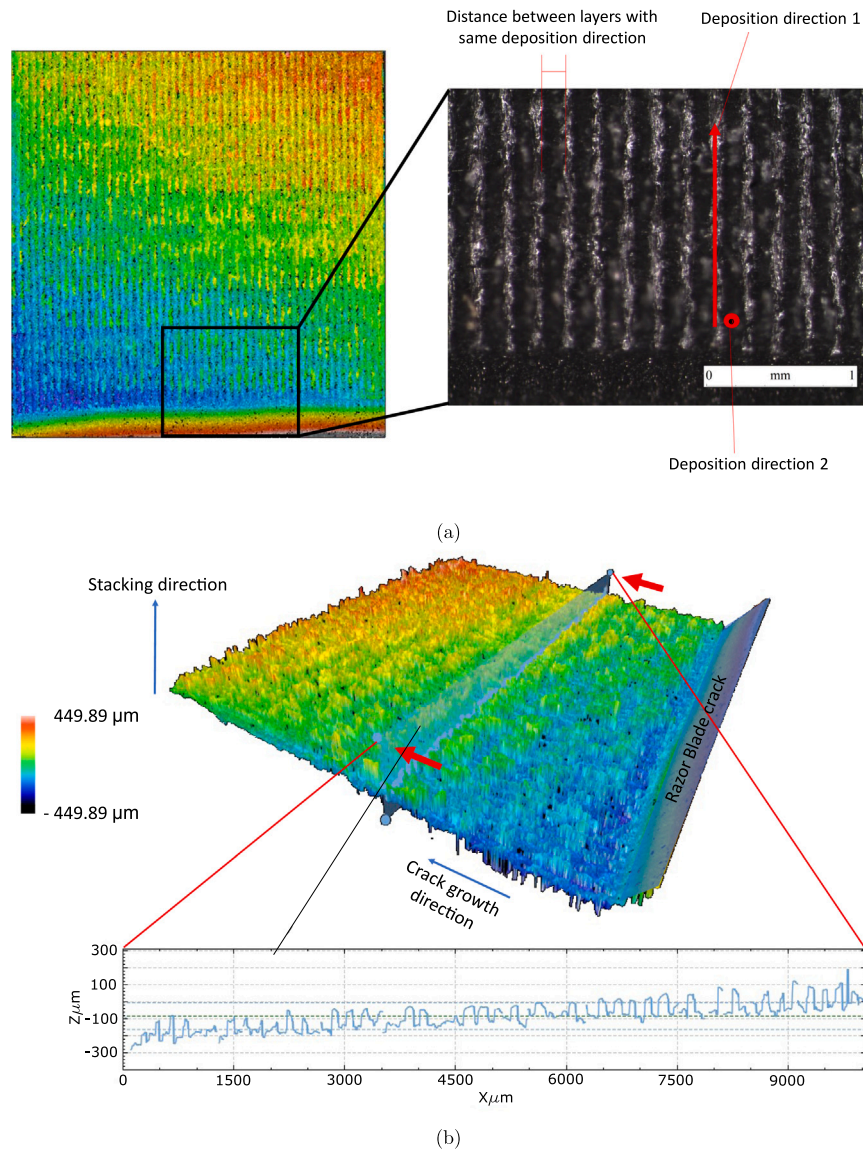
(a)

(b)

Fig. 10. Fracture surface from profilometer and microscope for the 45/−45 Horizontal configuration.

with 10x Nikon optic. Pictures of the crack paths and fracture surface obtained with the microscope for all configurations are shown in Figs. 4 and 5, respectively. In the following subsections, the digital images obtained from the digital profilometer are shown for each configuration. It is important to underline that the color legend in each image obtained with the digital profilometer is representative of the height of the fracture surface measured starting from the scanning midplane of the profilometer itself.

3.1.1. 0/90 Horizontal

An example of a tested specimen for this configuration is shown in Fig. 4(a) and the corresponding fracture surface, from the optical microscope, is shown in Fig. 5(a), while its digital reconstruction with the profilometer is shown in Fig. 6. In Fig. 6(a), the deposition direction for each layer (following the direction indicated by the raster angle) and the distance between the layers are clearly recognizable. The red dot in the picture is used to indicate a deposition direction which is perpendicular to the surface shown. Except for the regular high-frequency pattern corresponding to the layers, the fracture surface for this configuration is almost flat. In addition, the surface is almost horizontal, with a slight variation of altitude (from left to right of

the specimen). This is due to the non-perfect parallel-to-the-fracture-surface cut of the specimen during the post-mortem preparation for the profilometer. The upper part (red) has a higher altitude because it corresponds to the final split into two of the specimen, once out of the machine, and is not taken into account in the results. It can be noticed that it is perfectly planar if the rigid rotation is not taken into account, as shown in the bottom part of Fig. 6(b). Every peak in the plot indicates the transition between the layer of 0° and 90°.

As far as the other face of the same fracture surface is concerned, see Fig. 7, the results are the opposite of the previous, which means that no significant material was lost. The most illustrative part is the upper part of the face, that is now lower than the remaining, in order to perfectly fit with what was shown in Fig. 6. The same considerations made for the other face apply also in this case.

3.1.2. 0/90 Vertical

The results are now presented for the same lay-up but with a different deposition direction. An example of the post-mortem specimen is shown in Fig. 4(b) and the fracture surface in Fig. 5(b). The image of the same fracture surface recreated in a digital form by means of the profilometer is shown in Fig. 8. Similarly to the previous configuration, the deposition direction is clearly recognizable, see Fig. 8(a).
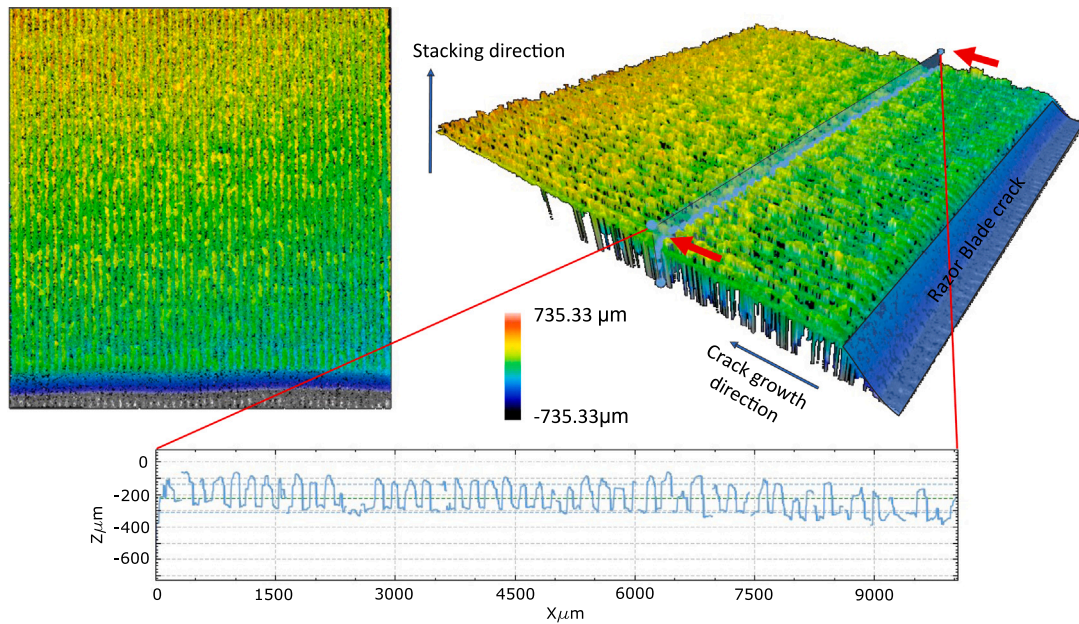
Fig. 11. Fracture surface from profilometer for the 45/−45 Horizontal configuration — opposite face.

The same considerations that apply to the previous configuration (0/90 Horizontal) are not valid anymore. In fact, the fracture surface is not flat, as clearly shown in Fig. 8(b). The crack, starting from the pre-crack created with the razor blade, does not have any preferential path fostered by the polymer deposition direction and, therefore, is free to open different crack surfaces involving different planes. This aspect justifies the change of plane of the crack in the middle of the fracture surface (highlighted by the red colored part in Fig. 8, which is at a higher altitude with respect to the remaining parts). The more freedom the crack has to create new surfaces, the higher the energy dissipated during the fracture process. This leads to an increase in the mechanical performance of this configuration with respect to the previous one.

As far as the other face of the same fracture surface is concerned, the results are identical and respectful of what was found so far. In particular, taking the images from the profilometer into account, as shown in Fig. 9, the central part of the face where the crack path changed plane to generate additional surfaces is now lower than the rest, which perfectly fits with what is shown in Fig. 8. This is also shown by comparing the profiles at the bottom of Fig. 8(b) and 9.

3.1.3. 45/−45 Horizontal

For this configuration, the analogous results are shown in Figs. 4(c) and 5(c).

In contrast to what happens for the cases analyzed in the previous sections, the fracture path is not following the initial direction of the pre-crack, but it follows a straight line with 45° orientation. This result is in agreement with what other authors in the literature observed when polymeric material is deposed with a raster angle of 45/−45° [32]. The fracture surface obtained is perfectly planar like the one obtained for the 0/90 Horizontal configuration, and there is no visible difference between the surfaces shown in Fig. 5(a) and (c). Therefore, all the conclusions that were deduced for the 0/90 Horizontal configuration are also valid for this one. In Figs. 10 and 11, the two faces of the same fracture surface are shown, showing perfect correspondence.

3.1.4. 45/−45 Vertical

This subsection discusses the analogous results but for a different deposition direction. Figs. 4(d) and 5(d) show an example of the tested specimen of this type and its fracture surface, respectively.

Similarly to the previous case, the crack obtained from the test does not follow a straight line. This is due again to the possibility for the crack to create multiple paths, as happened for the 0/90 Vertical configuration, thus justifying the increased mechanical properties with respect to its horizontal counterpart. The first surface is described in Fig. 12. Compared to the other three configurations presented so far, this one is by far the most complex. The extremely complex crack pattern is identical for all the five specimens tested with this configuration, thus giving the certainty of its physical meaning. The presence of multiple layers deposed, alternatively, at 45° and -45° gives the crack the possibility to branch multiple times and create a very complex fracture surface. It is important to underline how the different fracture planes are all inclined at 45°, as shown both in Figs. 12(b) and 13. The opposite face is shown in Figs. 14 and 15.

3.2. Experimental force–displacement curves

The experimental results of the SENB test in terms of Force– Displacement curves are shown in Fig. 16. All plots have the same vertical axis range to show the difference in the mechanical behavior among the four different printing configurations considered in this work. It is clear that for every configuration the specimens have very similar behavior, demonstrating the reliability of the printing and testing procedure. For the first three configurations (whose response is shown in Fig. 16(a),(b),(c)), the plots show a very low scatter among the different specimens both in the loading and damaging phase. The same consideration is not valid for the 45/−45 Vertical configuration (Fig. 16(d)). In fact, while the loading phase is basically identical for all the specimens, the damaging one, as well as the peak of the curves, shows a much larger scatter with respect to what is shown in the other configurations. This is due to what was anticipated in Section 3.1.4, where attention was focused on the multiple crack surfaces opened during the fracture process. The larger the number of possible crack surfaces that can be created, the more random the response of the specimen when damage occurs. This justifies the scatter in both peak load and post-damage response. By computing the average curves for each configuration, their performance can be compared in terms of improvement that the vertical deposition leads to. It is highlighted that for the 0/90 configuration, the adoption of a vertical deposition instead of a horizontal one leads to an improvement of the mechanical performance, in terms of peak load, of 45%. Instead, for the 45/−45 configuration, the switch leads to an improvement limited to 17%, demonstrating the initial superiority of the 45/−45 configuration with respect to the 0/90 one.
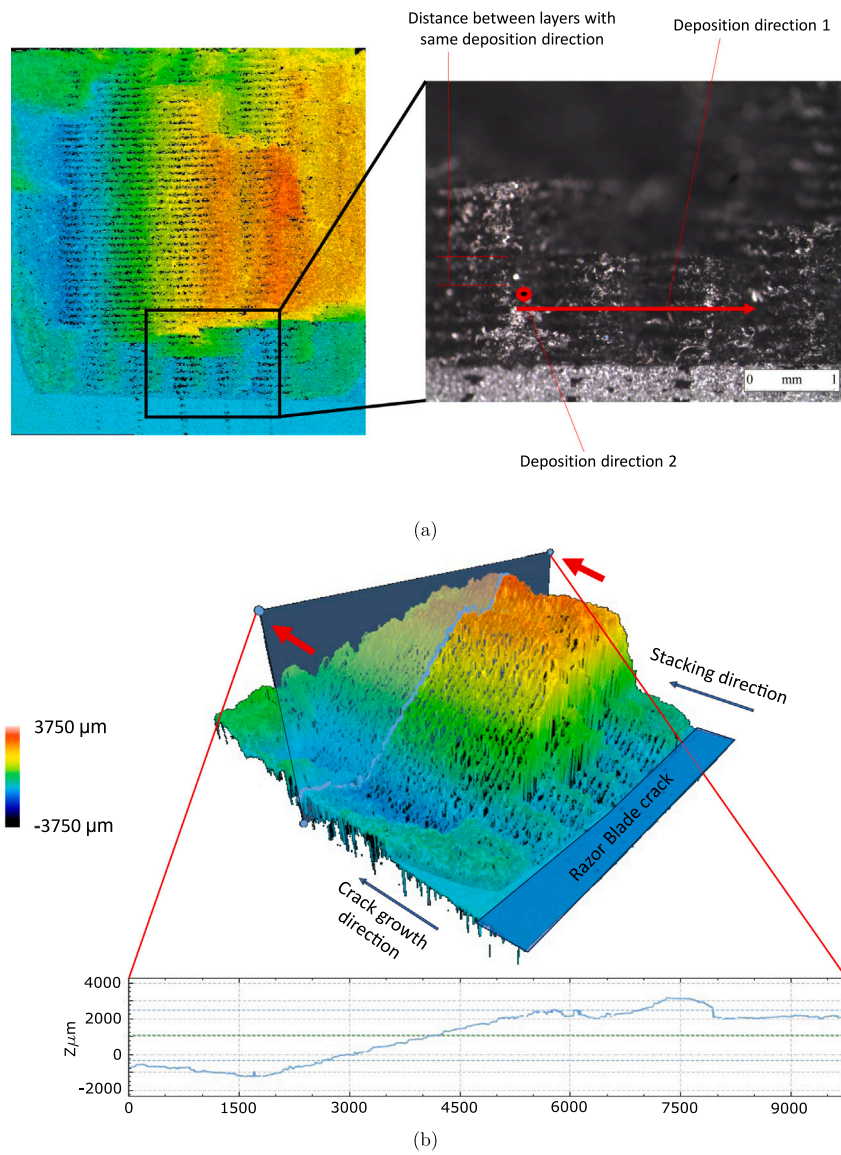
(a)

(b)

Fig. 12. Fracture surface from profilometer and microscope for the 45/−45 Vertical configuration.
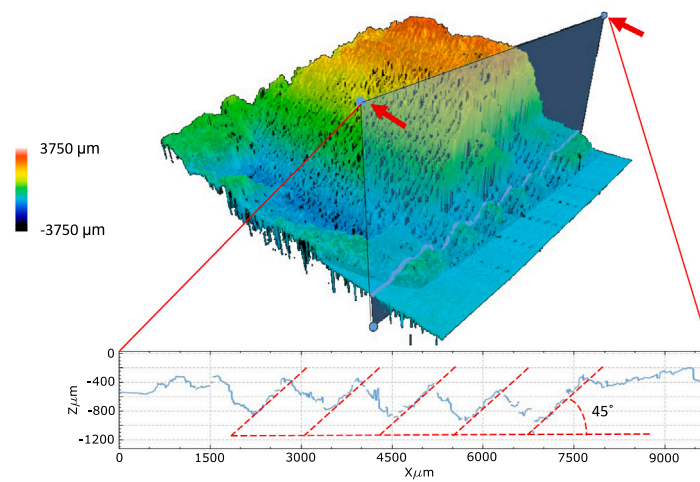

Fig. 13. Fracture surface from profilometer for the 45/−45 Vertical configuration — detail of the 45°.
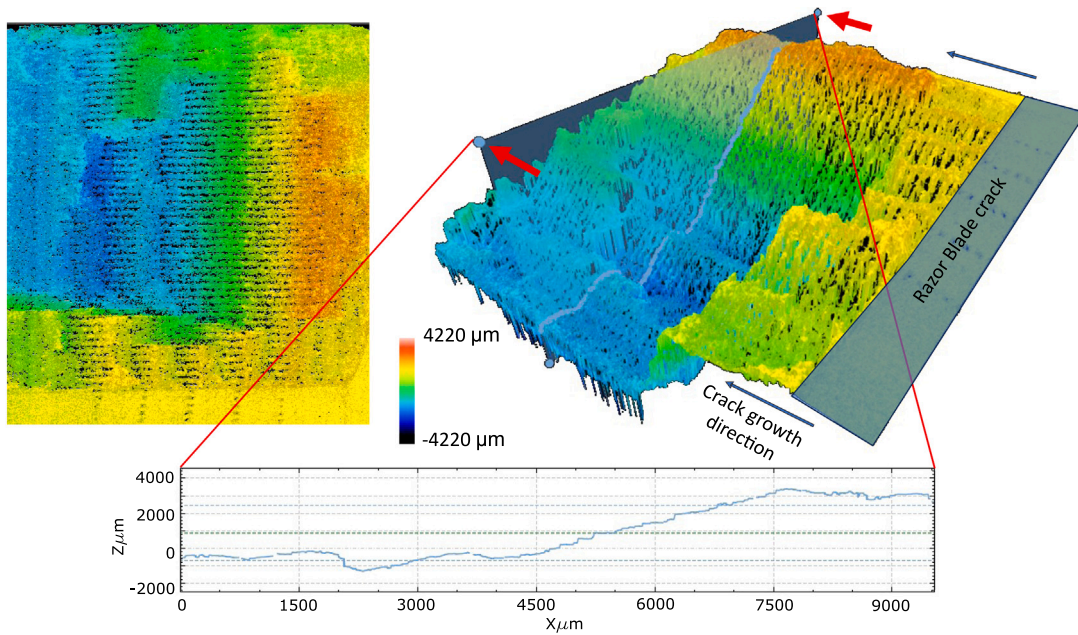
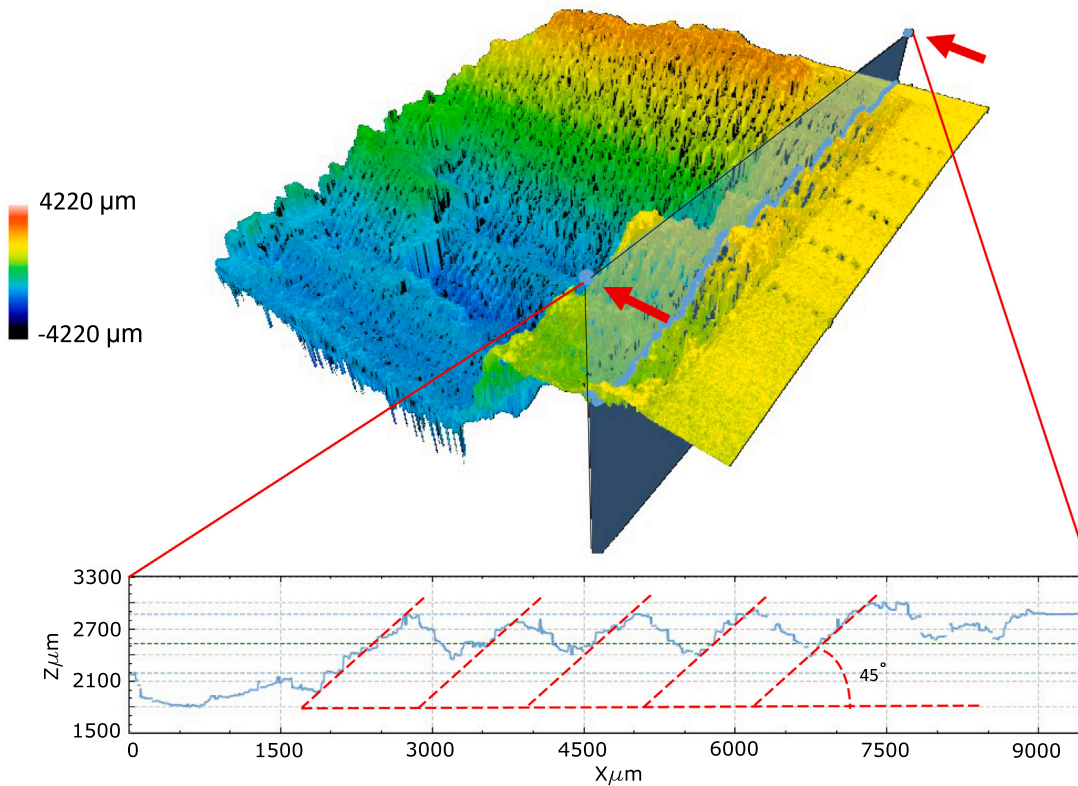**Fig. 14.** Fracture surface from profilometer for the 45/−45 Vertical configuration — opposite face.

Fig. 15. Fracture surface from profilometer for the 45/−45 Vertical configuration — opposite face, detail of the 45°.

4. Estimation of the critical stress intensity factor and the fracture toughness

This section aims at estimating the influence of the printing configuration on the fracture performance. First, the critical stress intensity

factor K_{Ic} is estimated using the ASTM D5045 standard [33]. Second, the fracture toughness G_{c} is estimated by integrating the force–displacement curve. Third, the roughness of the fracture surface is measured. Eventually, the experimental force–displacement curves are used to calibrate a cohesive model and estimate the fracture toughness corresponding to each configuration.
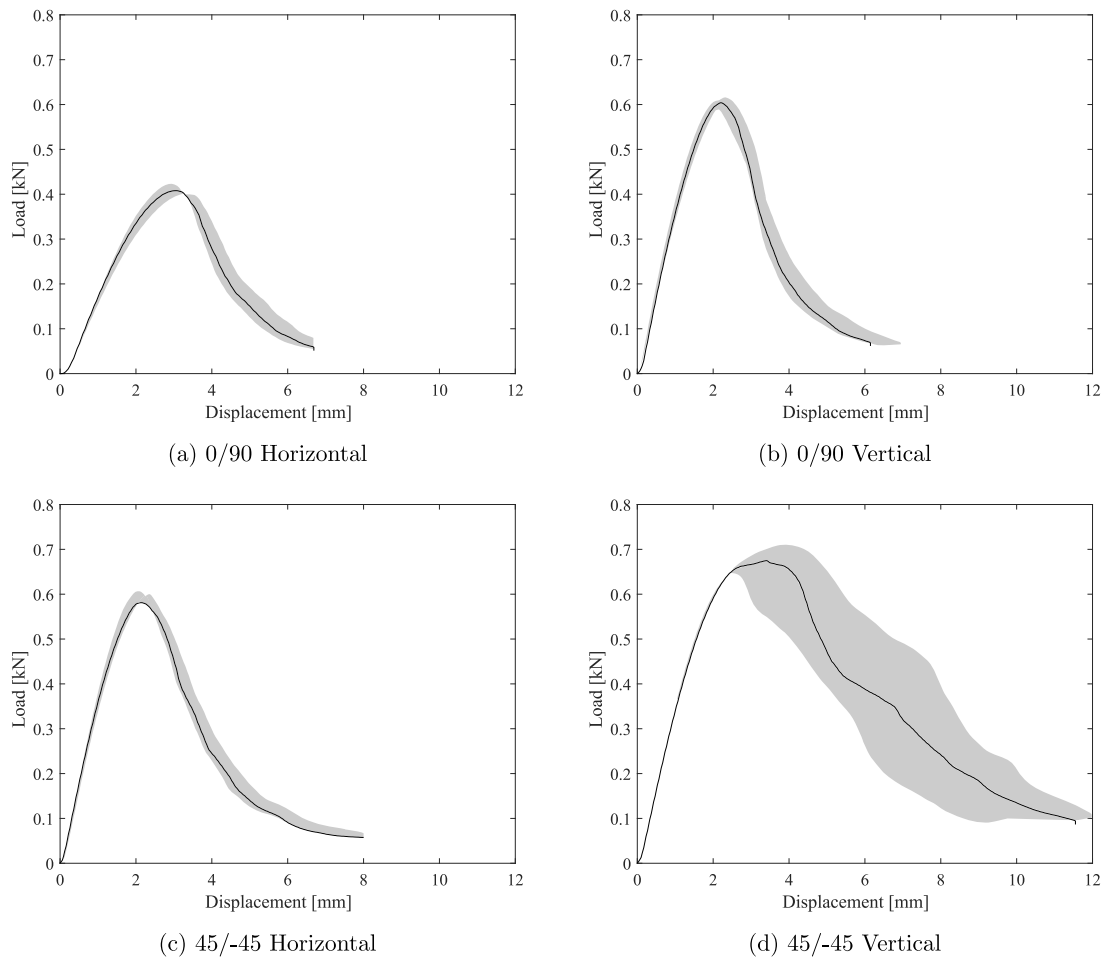
(a) 0/90 Horizontal

(b) 0/90 Vertical

(c) 45/-45 Horizontal

(d) 45/-45 Vertical

Fig. 16. Load–displacement curves for each studied configuration.

4.1. Estimation of the critical stress intensity factor using the ASTM D5045 standard

The standard ASTM D5045 [33] employs a reference load P_Q to estimate conditional K_{Ic} values. In this context, P_Q represents the load corresponding to the intersection of the load–displacement plot with a straight line having a slope equal to 95% of the initial slope of the load–displacement curve; see Fig. 17. According to the standard, load–displacement curves should have a large linear part followed by a short nonlinear behavior just before crack propagation occurs, both P_Q and the peak load P_{max} values should be similar within a margin. This condition is far from being fulfilled in this experiment. According to the standard, in this case, the specimens should be enlarged, but the required size is not compatible with the 3D printer available. Therefore, the estimations presented here should be taken as estimations not in accordance with the standard requirements and should be used only for qualitative comparison between configurations. By coherence the results obtained here will be denoted as pseudo critical stress intensity factor.

In the present study, K_Q^* and K_{max}^* are defined as the pseudo critical stress intensity factors obtained using P_Q and P_{max}, respectively, using the expressions given for K_Q in the ASTM D5045 standard [33].

In Fig. 18(a), the summary of K_Q^* values is presented, ranging from 1.69 to 3.12 MPa$\sqrt{m}$. Results indicate that +45/−45 configurations show a higher pseudo critical stress intensity factor compared to 0/90 configurations. Additionally, specimens printed in the vertical direction have higher values than those printed in the horizontal direction.

In Fig. 18(b), the summary of K_{max}^* values is shown, ranging from 3.06 to 5.72 MPa$\sqrt{m}$. Results also display that +45/−45 configurations
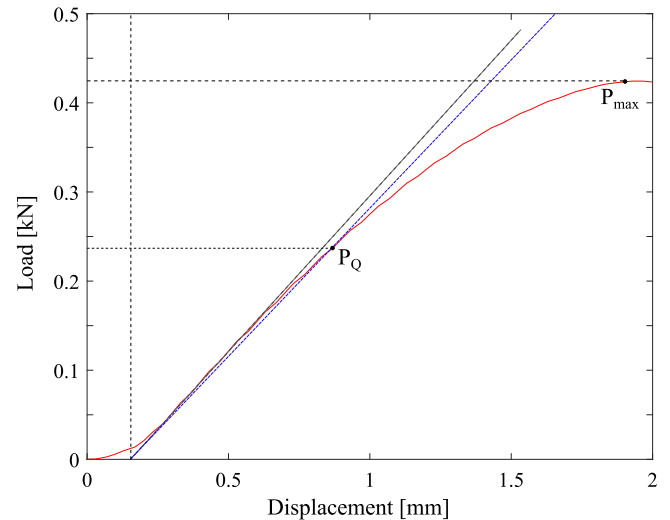

Fig. 17. Load vs. displacement for 0/90 Horizontal.

show a higher pseudo critical stress intensity factor compared to 0/90 configurations. Once again, specimens printed in the vertical direction have higher values than those printed in the horizontal direction.

Using P_{max}, the pseudo critical stress intensity factor presents higher values compared to the ones obtained using P_Q.
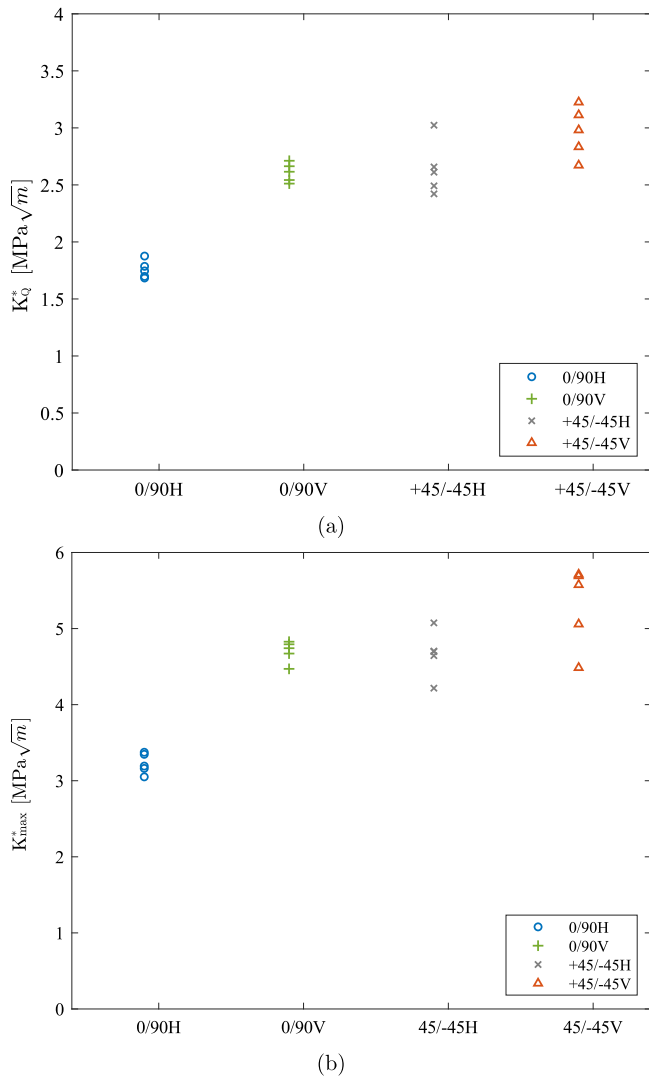
(a)

(b)

Fig. 18. Conditional fracture toughness as a function of four configurations under study, using (a) P_Q and (b) P_{max}, according to [33].

Fig. 19. Fracture toughness obtained from the experimental curves.
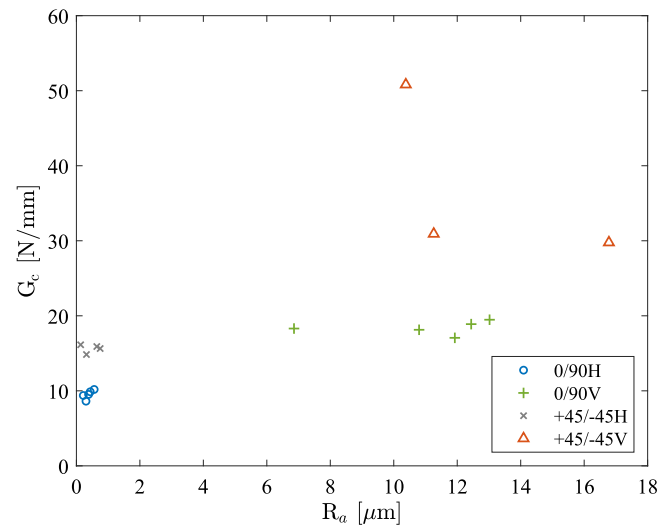
Fig. 20. Fracture toughness vs. arithmetic average surface roughness obtained from experiments.

4.2. Fracture toughness evaluation from force–displacement experimental curves

In this section, the fracture toughness is estimated through the experimental force–displacement curves shown in Fig. 16. A numerical integration is performed for every specimen, subtracting from the total integral the one corresponding to the unloading phase once the failure of the specimen occurs. Once the integral is computed, the fracture toughness is obtained dividing this integral by the crack surface area. The values of the fracture toughness obtained in this way for the different specimens are shown in Fig. 19.

As noticed by the comparison between Figs. 18 and 19, the trend between configurations is similar for fracture toughness and critical stress intensity factor. The large scatter in the 45/−45V configuration is justified by the one in the experimental curves, due to the mechanisms described in the section above.

4.3. Relation between fracture toughness and surface roughness

It is interesting to analyze if there is any relationship between the fracture toughness measured in the previous section, starting from the experimental curves, and the surface roughness of the postmortem fracture specimens. For each and every specimen whose fracture toughness
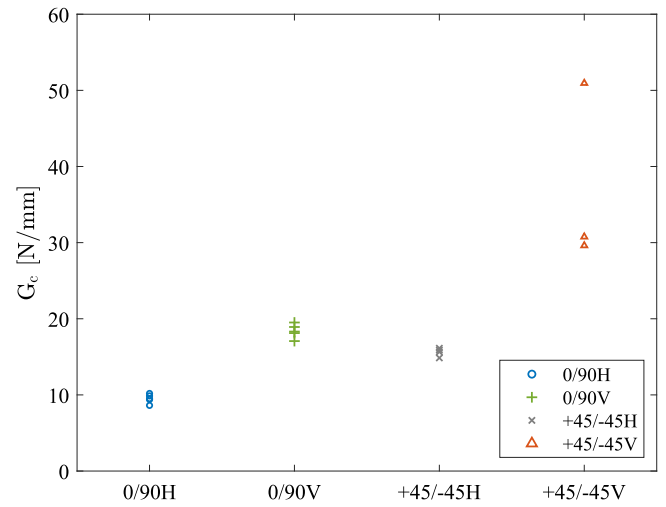
is shown in Fig. 19, the surface roughness was measured using a TR100 Surface Roughness Tester. The correlation between the two quantities is shown in Fig. 20.

It is clearly shown that no direct relation is present, which would imply that to each value of roughness corresponds one value of fracture toughness. Indeed, specimens with configurations 0/90H and 45/−45H have a very similar roughness, also supported by the observation of the fracture surface for the two specimens in Section 3, but the value of fracture toughness is almost double. Therefore, it is straightforward to conclude that the fracture toughness is dependent not only on the value of the roughness of the surface, but also on the raster angle used for the deposition and the stacking direction, all factors that deeply influence the crack pattern. It is also clear how the configurations obtained with a vertical stacking direction are characterized by higher roughness with respect to their horizontal counterpart.

4.4. Estimation of the fracture toughness by matching with numerical simulations

The values obtained for the critical stress intensity factor in Section 4.1 are not representative of the critical value since, as described
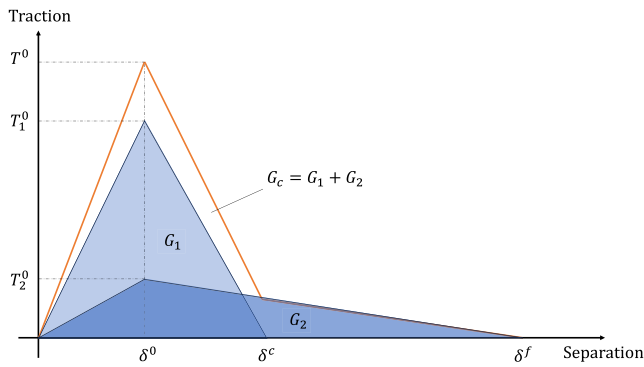
Fig. 21. Bilinear law for the cohesive elements.

Table 1
Cohesive properties for pure Mode I crack propagation.

	G_1 [N/mm]	G_2 [N/mm]	G_c [N/mm]	T_1 [MPa]	T_2 [MPa]
0/90H	8	4	12	40	10
0/90V	18	5	23	40	10
45/−45V	25	10	35	40	10

in the section itself, the experimental curves, although representative of the material behavior, were obtained with specimens too small to get an initial straight line response in the force–displacement curve which would have allowed to obtain the values of critical stress intensity factors according to the standard ASTM 5045. Therefore, a numerical simulation is used to catch the correct value of fracture toughness, trying to capture the experimental trend obtained in the experiments.

4.4.1. Model set-up and results

To model numerically the SENB, the Finite Element (FE) software Abaqus has been used. Plane strain elements CPE4 were used and displacement on the top node was imposed to replicate the experimental loading conditions. Cohesive elements deposed along the expected crack line (observed experimentally) to model crack propagation and a bilinear softening law is adopted, see Fig. 21. The overall G_c, which is equal to the sum of G_1 and G_2, corresponding to the two layers of cohesive elements superimposed on the crack path, defines the softening behavior after the peak load has been reached. This last one is obtained by tuning the values of G_1 and G_2 in a way that their summation (G_c) always gives the same value, in order to obtain the proper softening behavior.

The results of the numerical simulations, along with a comparison with the experimental results, are shown in Fig. 22. The values of G_c, G_1 and G_2, as long as the values of the critical stresses of the cohesive law for the different configurations, are resumed in Table 1.

These properties refer to Mode I propagation, which clearly appears in the configurations 0/90H, 0/90V and 45/−45V. In case of the 45/−45H configuration, a mixed mode crack propagation takes place. The properties of the cohesive elements used in the numerical simulation to catch numerically the experimental results in case of mixed mode are: $G_{I1} = 11$ N/mm, $G_{II1} = 10$ N/mm, $G_{I2} = 4$ N/mm, $G_{II2} = 10$ N/mm, $T_{norm1} = 15$ MPa, $T_{shear1} = 15$ MPa, $T_{norm2} = 10$ MPa, $T_{shear2} = 10$ MPa, the coefficient for the BK law is equal to 2.1.

The numerical results show a very good correlation with the experiments, giving confidence that the model has been set up with the correct value of fracture toughness. Furthermore, the fracture toughness values assigned to the cohesive elements to replicate the experimental results are in accordance with the values computed in Section 4.2 by integrating the force–displacement curves.

5. Conclusions

In this work, the influence of different printing parameters, such as stacking direction and raster angle, on the fracture performance of SENB specimens printed in Onyx is studied. Four different printing configurations are adopted to manufacture the same specimen, 0/90H, 0/90V, 45/−45H and 45/−45V. All configurations are tested in the same way and their mechanical response is compared. It is shown that the specimens printed with a vertical stacking direction (indicated by the letter V) have always a superior mechanical response compared to the one of their horizontal counterpart (indicated by the letter H), showing an improvement in the maximum load attainable by the structure. In particular, as shown in the Force–Displacement curves of Fig. 16, the best configuration to be used to print a specimen is the 45/−45V one, due to the possibility to open many fracture surfaces during the failure process, thus increasing the energy dissipation and therefore, the toughness. This is clearly shown by a detailed comparison among the fracture surfaces for all the specimens and configurations. The fracture toughness is measured for each specimen starting from the experimental curves obtained, highlighting that the vertical configurations show an improvement due to the mechanisms mentioned above. Again, as stated above, the 45/−45V configuration shows the highest fracture toughness value. Lastly, the roughness is measured, concluding that there is no direct and univocal relation between the fracture toughness of a specimen and the roughness of its fracture surface. Therefore, it is not possible to deduce the toughness value only by measuring the surface roughness. This work sheds a light on the toughening mechanisms which can be achieved by means of the 3D printing technology by solely choosing an appropriate combination of stacking direction and raster angle, preserving the shape of the component. Such study underlines the importance that this technology might have on the development of tougher components to be adopted in any field where safety is of primary importance, such as aerospace, automotive or mechanical devices. It is important to underline that this work is limited to the analysis of components realized in Onyx, without taking into consideration the presence of continuous fiber reinforcement. The addition of such reinforcement could influence the damage mechanisms involved in the failure process of the specimen. Therefore, a possible development could be the extension of this work to components printed with continuous fibers, considering different reinforcement materials available for 3D printing, such as carbon fiber, glass fiber or Kevlar®. Also in this case, the measurement of quantities such as fracture toughness and surface roughness are of great importance for the community, especially when numerical simulations come into play, needing accurate values for the fracture properties.

CRediT authorship contribution statement

Simone Sangaletti: Conceptualization, Data curation, Formal analysis, Investigation, Methodology, Writing – original draft, Writing – review & editing. **María Teresa Aranda:** Conceptualization, Data curation, Formal analysis, Investigation, Writing – original draft, Writing – review & editing. **Luis Távara:** Conceptualization, Methodology, Supervision, Writing – review & editing. **Israel García García:** Conceptualization, Methodology, Supervision, Writing – review & editing.

Declaration of competing interest

The authors declare that they have no known competing financial interests or personal relationships that could have appeared to influence the work reported in this paper.

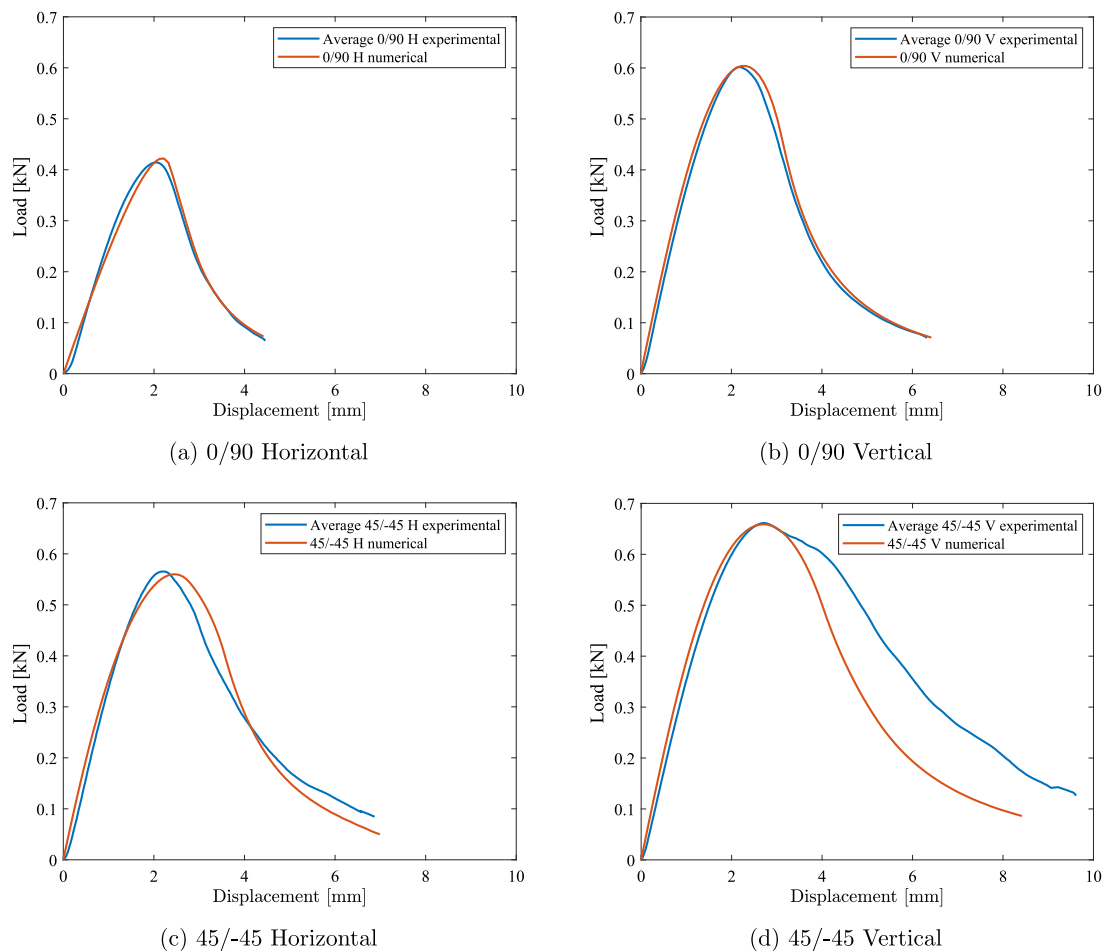## Data availability

Data will be made available on request.

(a) 0/90 Horizontal

(b) 0/90 Vertical

(c) 45/-45 Horizontal

(d) 45/-45 Vertical

Fig. 22. Load–displacement curves, comparison between simulation and experimental results.

Acknowledgments

References

[1] X. Wang, M. Jiang, Z. Zhou, J. Gou, D. Hui, 3D printing of polymer matrix composites: A review and prospective, Composites B 110 (2017) 442–458.

[2] S.M.F. Kabir, K. Mathur, A.-F.M. Seyam, A critical review on 3D printed continuous fiber-reinforced composites: History, mechanism, materials and properties, Compos. Struct. 232 (2020) 111476.

[3] V. Giurgiutiu, Structural health monitoring (SHM) of aerospace composites, in: P. Irving, C. Soutis (Eds.), Polymer Composites in the Aerospace Industry, Woodhead Publishing, 2015, pp. 449–507.

[4] S. Kupczyk, Supportability of composite airframes: Civilian and military aspects, Compos. Struct. 10 (1) (1988) 37–50, Special Issue Supportability of Composite Air Frames.

[5] C. Soutis, Carbon fiber reinforced plastics in aircraft construction, Mater. Sci. Eng. A 412 (1) (2005) 171–176, International Conference on Recent Advances in Composite Materials.

[6] S.C. Joshi, A.A. Sheikh, 3D printing in aerospace and its long-term sustainability, Virtual Phys. Prototyp. 10 (4) (2015) 175–185.

[7] P. Morgan, Carbon Fibers and their Composites, CRC Press, Boca Raton, Florida, 2005.

[8] L.J. Love, V. Kunc, O. Rios, C.E. Duty, A.M. Elliott, B.K. Post, R.J. Smith, C.A. Blue, The importance of carbon fiber to polymer additive manufacturing, J. Mater. Res. 29 (17) (2014) 1893–1898.

[9] J. Justo, L. Távara, L. García-Guzmán, F. París, Characterization of 3D printed long fibre reinforced composites, Compos. Struct. 185 (2018) 537–548.

[10] A.D. Pertuz, S. Díaz-Cardona, O.A. González-Estrada, Static and fatigue behaviour of continuous fibre reinforced thermoplastic composites manufactured by fused deposition modelling technique, Int. J. Fatigue 130 (2020) 105275.

[11] M.A. Caminero, J.M. Chacón, I. García-Moreno, J.M. Reverte, Interlaminar bonding performance of 3D printed continuous fibre reinforced thermoplastic composites using fused deposition modelling, Polym. Test. 68 (2018) 415–423.

[12] M.A. Caminero, J.M. Chacón, I. García-Moreno, G.P. Rodríguez, Impact damage resistance of 3D printed continuous fibre reinforced thermoplastic composites using fused deposition modelling, Composites B 148 (2018) 93–103.

[13] M.T. Aranda, J. Reinoso, I.G. García, On different 3D printing methods and fracture performance in DCB composite specimens including structured interfaces, Theor. Appl. Fract. Mech. 122 (2022) 103552.

[14] Z.Z. Pan, L.W. Zhang, K.M. Liew, A phase-field framework for failure modeling of variable stiffness composite laminae, Comput. Methods Appl. Mech. Engrg. 388 (2022) 114192.

[15] S. Sangaletti, I. García, Fracture tailoring in 3D printed continuous fibre composite materials using the phase field approach for fracture, Compos. Struct. 300 (2022) 116127.

[16] S. Sangaletti, A. Mitrou, I.G. García, A. Arteiro, Effect of tailored fiber deposition in 3D printed composites: application of an anisotropic phase field model, Theor. Appl. Fract. Mech. 127 (2023) 104030.

[17] P. Li, J. Yvonnet, C. Combescure, H. Makich, M. Nouari, Anisotropic elastoplastic phase field fracture modeling of 3D printed materials, Comput. Methods Appl. Mech. Engrg. 386 (2021) 114086.

[18] M.R. Khosravani, S. Rezaei, H. Ruan, T. Reinicke, Fracture behavior of anisotropic 3D-printed parts: experiments and numerical simulations, J. Mater. Res. Technol. 19 (2022) 1260–1270.

[19] R. Mattey, B. Jewell, S. Ghosh, T. Sain, Phase-field fracture coupled elasto-plastic constitutive model for 3D printed thermoplastics and composites, Eng. Fract. Mech. 291 (2023) 109535.

[20] J. Russ, V. Slesarenko, S. Rudykh, H. Waisman, Rupture of 3D-printed hyperelastic composites: Experiments and phase field fracture modeling, J. Mech. Phys. Solids 140 (2020) 103941.

[21] A. Estefani, L. Távara, Numerical multiscale analysis of 3D printed short fiber composites parts: Filament anisotropy and toolpath effects, Eng. Rep. (2023) e12799.

[22] L. Marşavina, D.I. Stoia, L. Emanoil, Fracture toughness in additive manufacturing by selective laser sintering: an overview, Mater. Des. Process. Commun. 3 (6) (2021) 1–7.

[23] E. Linul, L. Marsavina, D.I. Stoia, Mode I and II fracture toughness investigation of laser-sintered polyamide, Theor. Appl. Fract. Mech. 106 (2020) 102497.

[24] I.I. Cuesta, E. Martinez-Pañeda, A. Díaz, J.M. Alegre, The essential work of fracture parameters for 3D printed polymer sheets, Mater. Des. 181 (2019).

[25] Z. Quan, J. Suhr, J. Yu, X. Qin, C. Cotton, M. Mirotznik, T.-W. Chou, Printing direction dependence of mechanical behavior of additively manufactured 3D preforms and composites, Compos. Struct. 184 (2018) 917–923.

[26] J.M. Chacón, M.A. Caminero, E. García-Plaza, P.J. Núñez, Additive manufacturing of PLA structures using fused deposition modelling: Effect of process parameters on mechanical properties and their optimal selection, Mater. Des. 124 (2017) 143–157.

[27] D. Yadav, P. Gupta, B.N. Jaya, Impact of build direction, infill pattern and raster angle on mechanical properties and damage tolerance of 3D printed PLA, in: Proceedings of the 2022 International Additive Manufacturing Conference, in: International Manufacturing Science and Engineering Conference, 2022, V001T01A004.

[28] F. Arbeiter, M. Spoerk, J. Wiener, A. Gosch, G. Pinter, Fracture mechanical characterization and lifetime estimation of near-homogeneous components produced by fused filament fabrication, Polym. Test. 66 (2018) 105–113.

[29] N. Aliheidari, R. Tripuraneni, A. Ameli, S. Nadimpalli, Fracture resistance measurement of fused deposition modeling 3D printed polymers, Polym. Test. 60 (2017) 94–101.

[30] R. Zou, Y. Xia, S. Liu, P. Hu, W. Hou, Q. Hu, C. Shan, Isotropic and anisotropic elasticity and yielding of 3D printed material, Composites B 99 (2016) 506–513.

[31] M.R. Khosravani, M.R. Ayatollahi, T. Reinicke, Effects of post-processing techniques on the mechanical characterization of additively manufactured parts, J. Manuf. Process. 107 (2023) 98–114.

[32] L. Távara, C. Madrigal, M.T. Aranda, J. Justo, Anisotropy and ageing effect on the mechanical behaviour of 3D-printed short carbon-fibre composite parts, Compos. Struct. 321 (2023) 117196.

[33] D5054, Standard test methods for plane-strain fracture toughness and strain energy release rate of plastic materials, Annu. Book ASTM Stand. 99 (Reapproved) (1996) 1–9.

[34] K. Rajan, M. Samykano, K. Kadirgama, W.S.W. Harun, M.M. Rahman, Fused deposition modeling: process, materials, parameters, properties, and applications, Int. J. Adv. Manuf. Technol. 120 (3–4) (2022) 1531–1570.